Electronic Supplementary Material (ESI) for Physical Chemistry Chemical Physics.

Self-Assembling, Structure and Nonlinear Optical Properties of Fluorescent Organic Nanoparticles in Water: Supporting Information

Laurie Lescos, Pierre Beaujean, Claire Tonnelé, Philippe Aurel, Mireille Blanchard-Desce, Vincent Rodriguez, Marc de Wergifosse, Benoît Champagne, Luca Muccioli, and Frédéric Castet

Contents

I. Force field parameterization and MD simulations

1. Validation of the force field used for water

In order to validate the force field used to describe water, preliminary MD simulations were run for pure solvent molecules, from which key physical observables were extracted and compared to experimental data. Bulk properties such as the mass density and local structure were first calculated. The mass density ρ_m is defined as:

$$\rho_m = \frac{ZM}{N_A V}$$

where Z is the number of molecules in the simulation box, M is the molar mass of the water molecule, N_A is the Avogadro constant and V is the volume of the simulation box. The local structure is characterized by radial distribution functions (RDF) $g(r)$ between atoms or mass centers of molecules, given by:

$$g(r) = \frac{N(r, r+dr)}{\frac{Z}{V} 4\pi r^2 dr}$$

where N is the number of water molecules at a distance comprised between r and $r + dr$ from a reference one. As shown in Table S1 and Figure S1, the water model SPC/Fw [S1] reproduces very well the mass density and water bulk properties, giving results very close to the experimental ones.

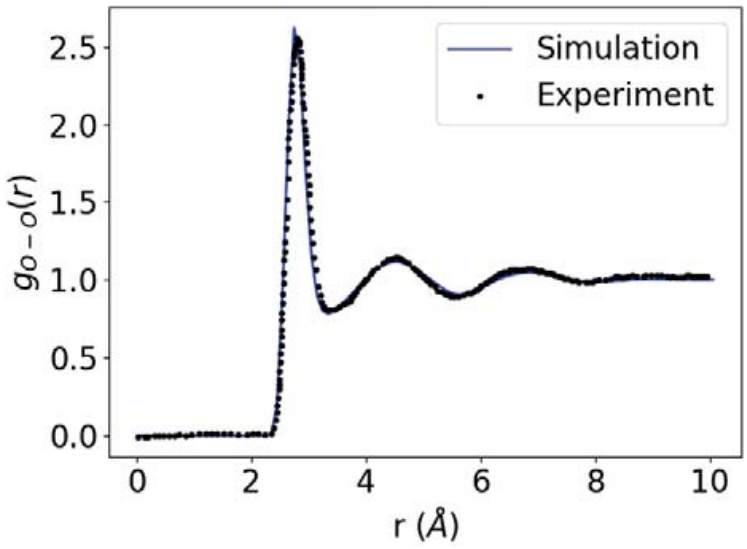

Figure S1: RDF between oxygens at 300 K, comparing simulation and experiment. Simulations at equilibrium were run for 20 ns on a box of 500 solvent molecules, using the NpT ensemble at p = 1.01325 bar. Experimental data were extracted from reference [S2].

The self-diffusion coefficient and the static dielectric constant, which are directly related to the solvent dynamics and solvent-mediated electrostatic interactions, were also evaluated. The self-diffusion coefficient D is defined by:

$$D = \lim_{n\to\infty} \frac{1}{6t} \langle [\boldsymbol{r}(t) - \boldsymbol{r}(0)]^2 \rangle$$

where t is the elapsed time, $\boldsymbol{r}$ is the position of all particles and $\langle [\boldsymbol{r}(t) - \boldsymbol{r}(0)]^2 \rangle$ is the mean square displacement. The static dielectric constant ε can be written as:

$$\varepsilon = 1 + \frac{1}{3\varepsilon_0} \frac{\sum_i \mu_i}{V k_B T} + \frac{N\alpha}{V\varepsilon_0}$$

where ε_0 is the vacuum permittivity, μ_i is the dipole moment of the water molecule, V is the volume of the simulation box, k_B is the Boltzmann constant, T is the temperature, N is the number of solvent molecules and α is the molecular polarizability. The second term in the right-hand side describes the permanent dipole contribution, while the last term describes the induced dipole contribution. The latter term is neglected in non-polarizable force fields. Results presented in Table 1 show that all the experimental and calculated values of the self-diffusion coefficient and static dielectric constant are in the same range.

Moreover, the self-diffusion activation energy was deduced from the self-diffusion coefficient D, which follows an Arrhenius-like relation with temperature T: [S3]

$$\ln D = \ln D_0 - \frac{E_A}{k_B T}$$

where E_A is the self-diffusion activation energy, D_0 is the diffusion coefficient at infinite temperature. The calculated activation energy, deduced from the linear evolution of the self-diffusion coefficient as a function of the reciprocal of temperature, is very close to the experimental value (Table 1).

Table S1: Calculated and experimental physical properties of water at T = 300 K. Simulations at equilibrium were run for 20 ns on a box of 500 solvent molecules, using the NpT ensemble at p = 1.01325 bar. Experimental data are from references [S4] and [S5].

Physical property	Calc.	Exp.
$\rho_m \ (g/cm^3)$	1.002	0.997
$D \ (10^{-8} m^2/s)$	0.231	0.245
ε	80.0	77.4
$E_A (kJ/mol)$	17	18

2. Torsional energy profiles of organic chromophores

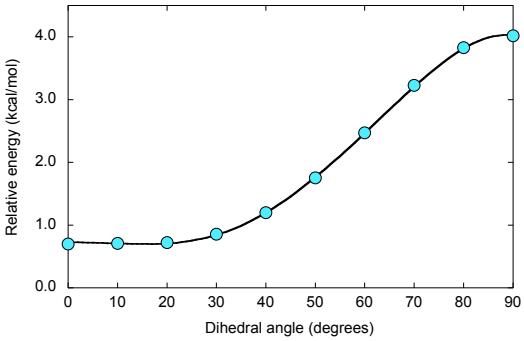

Figure S2a: Comparison of the free energy profile associated to the rotation around the Thienyl-Thienyl dihedral angle (ϕ_{TT} = S-C-C-S, see Figure 1 of the main text), obtained at the B3LYP/cc-pVTZ level in gas phase at T = 300K (dots) and using the reparametrized force field (line).

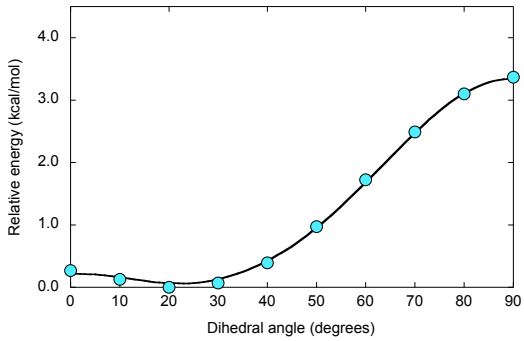

Figure S2b: Comparison of the free energy profile associated to the rotation around the Thienyl-Phenyl dihedral angle (ϕ_{TP}, see Figure 1 of the main text), obtained at the B3LYP/cc-pVTZ level in gas phase at T = 300K (dots) and using the reparametrized force field (line).

3. MD simulations of organic chromophores in water

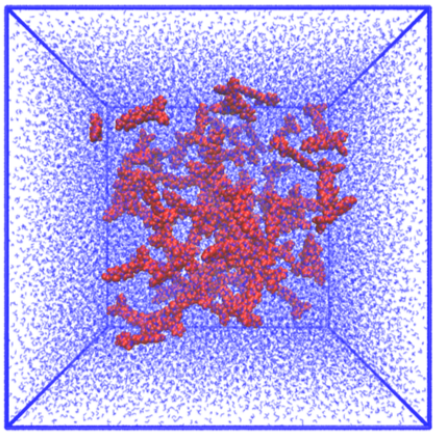

Figure S3: Starting configuration of the 8 simulations in pure water.

II. Determination of the optimal parameters of the sTD-DFT method

This section reports calculations of the first hyperpolarizability of the isolated dye in three different geometries randomly extracted from the MD trajectory (Figure S4a), and on a supramolecular cluster containing 12 chromophores (Figure S4b). These benchmarks have for objective of defining the optimal values of the y_J and y_K parameters used to damp the two-electron Coulomb and exchange integrals (equations 2-3, main text). The energy threshold E_{th} used to truncate the number of configuration state functions in the SCI (Configuration Interaction Singles) procedure is also optimized.

1. Test molecular and supramolecular geometries

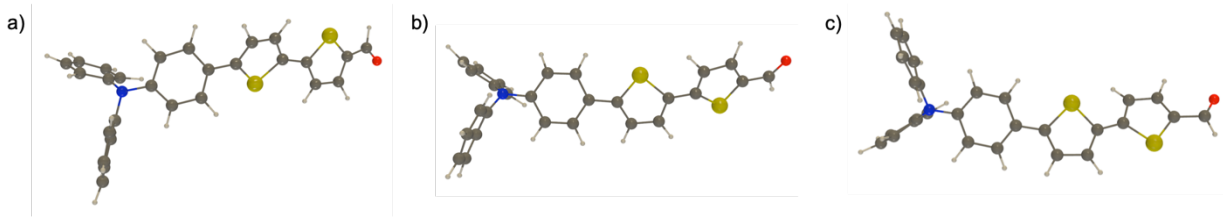

Figure S4a: Different geometries of the isolated dyes considered in the sTD-DFT benchmarks.

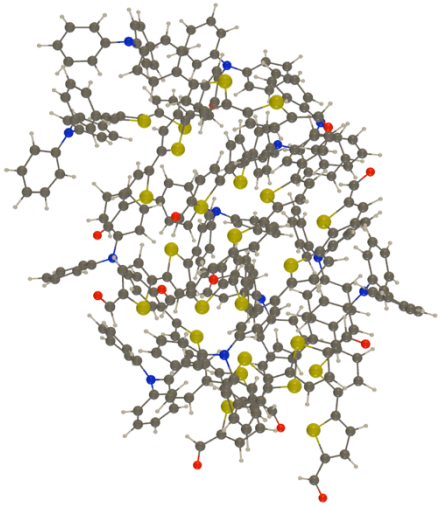

Figure S4b: Geometry of the aggregate composed of 12 dyes considered in the sTD-DFT benchmarks.

2. Optimization of the sTD-DFT-xTB parameters

In this Section, the y_J and E_{th} parameters of the sTD-DFT-xTB method are adjusted by comparison to reference TD-DFT/M06-2X/6-311G(d) calculations in gas phase, while y_K is kept fixed to its default value of 2.0. The y_J parameter is first tuned on the three test geometries of the isolated molecule (Figures S5, S6 and S7). It can be observed that default parameter value $y_J = 4.0$ satisfactorily reproduces the evolution of the first hyperpolarizabilities with the energy of the incident light ($E = \hbar\omega$), as calculated using the reference TD-DFT level. Numerical β values calculated at the TD-DFT and sTD-DFT-xTB levels using ω = 0.000 eV, ω = 0.827 eV and ω

= 1.165 eV are reported in Table S2. For ω = 1.165 eV, the absolute errors of the sTD-DFT-xTB approach compared to the TD-DFT reference are lower than 5% whatever the geometry. Smaller ω values lead to larger errors, which however remain acceptably small (< 17%).

In a second step, we addressed the impact of varying the energy threshold in sTD-DFT-xTB calculations, using default parameters. As shown in Figures S8, S9 and S10 for the isolated molecules, the frequency dispersion curves of the first hyperpolarizabilities calculated using sTD-DFT-xTB are downshifted compared to reference TD-DFT calculations. Moreover, reducing E_{th} from 10 to 6 eV negligibly impacts the sTD-DFT-xTB results, while those obtained with E_{th} = 5.0 eV show larger deviations. A similar conclusion can be drawn for calculations performed for the supramolecular aggregate (Figure S11). Therefore, an energy threshold value of E_{Th} = 6.0 eV can be used to minimize the calculation time in sTD-DFT-xTB calculations without any significant loss of accuracy.

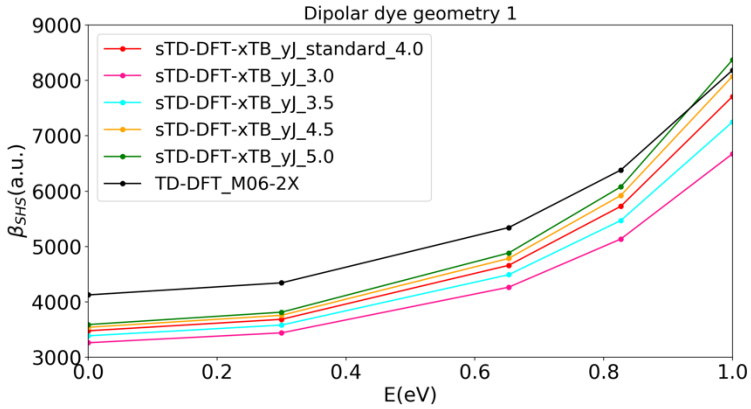

Figure S5: Tuning of the y_J parameter for the geometry 1 of the isolated molecule (Fig. S4a). In all sTD-DFT-xTB calculations, y_K = 2.0 and E_{Th} = 10 eV.

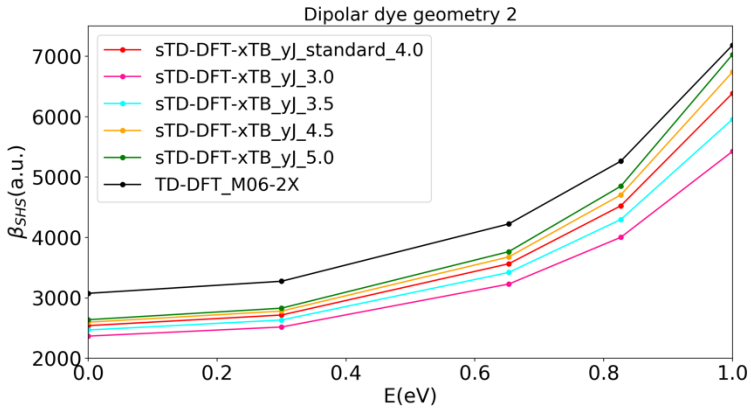

Figure S6: Tuning of the y_J parameter for the geometry 2 of the isolated molecule (Fig. S4a). In all sTD-DFT-xTB calculations, y_K = 2.0 and E_{Th} = 10 eV.

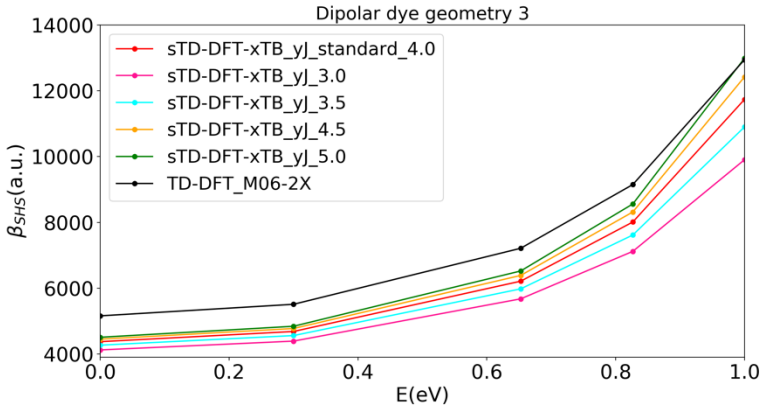

Figure S7: Tuning of the y_J parameter for the geometry 3 of the isolated molecule (Fig. S4a). In all sTD-DFT-xTB calculations, $y_K = 2.0$ and $E_{Th} = 10$ eV.

Table S2: Comparison between static and dynamic first hyperpolarizabilities calculated at the sTD-DFT-xTB and TD-DFT levels for the three test geometries of the isolated molecule shown Figure S4a. First hyperpolarizabilities β are calculated at three different excitation energies ω. In all sTD-DFT-xTB calculations, $y_J = 4.0$, $y_K = 2.0$ and $E_{Th} = 10$ eV.

Geometry 1

β(-2ω; ω,ω)	sTD-DFT-xTB	TD-DFT	error
ω = 0.000 eV	3 478	4 126	-16%
ω = 0.827 eV	5 727	6 381	-10%
ω = 1.165 eV	11 827	11 490	+3%

Geometry 2

β(-2ω; ω,ω)	sTD-DFT-xTB	TD-DFT	error
ω = 0.000 eV	2 540	3 075	-17%
ω = 0.827 eV	4 524	5 263	-14%
ω = 1.165 eV	10 524	11 063	-5%

Geometry 3

β(-2ω; ω,ω)	sTD-DFT-xTB	TD-DFT	error
ω = 0.000 eV	4 374	5 159	-15%
ω = 0.827 eV	8 012	9 151	-12%
ω = 1.165 eV	21 439	21 613	-1%

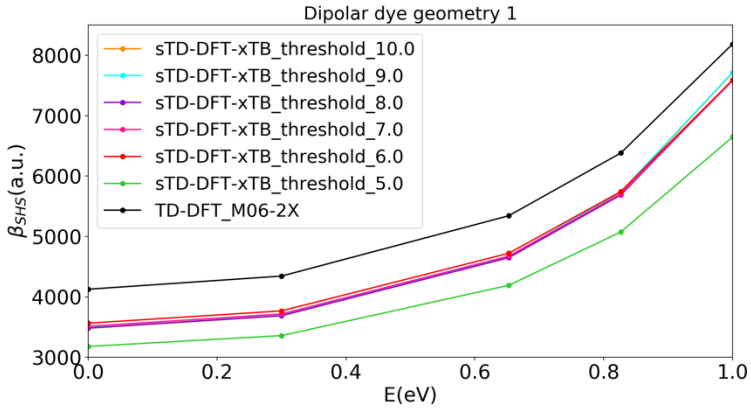

Figure S8: Tuning of the energy threshold E_{Th} for the geometry 1 of the isolated molecule (Fig. S4a). In all sTD-DFT-xTB calculations, $y_J = 4.0$ and $y_K = 2.0$.

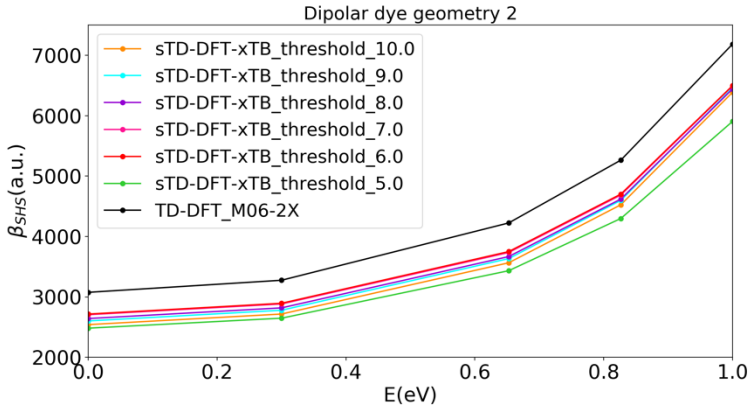

Figure S9: Tuning of the energy threshold E_{Th} for the geometry 2 of the isolated molecule (Fig. S4a). In all sTD-DFT-xTB calculations, $y_J = 4.0$ and $y_K = 2.0$.

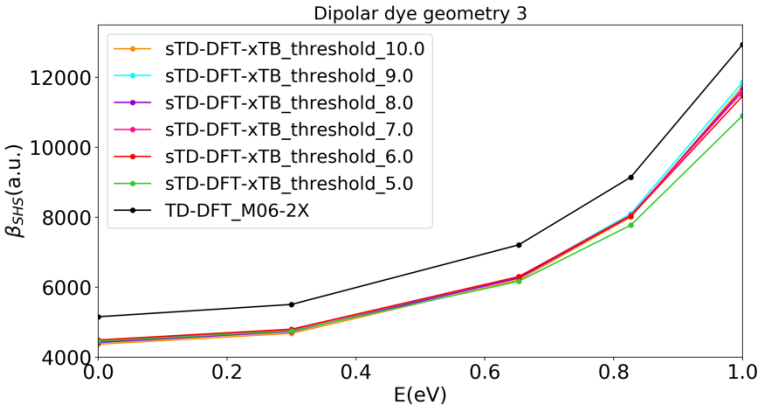

Figure S10: Tuning of the energy threshold E_{Th} for the geometry 3 of the isolated molecule (Fig. S4a). In all sTD-DFT-xTB calculations, $y_J = 4.0$ and $y_K = 2.0$.

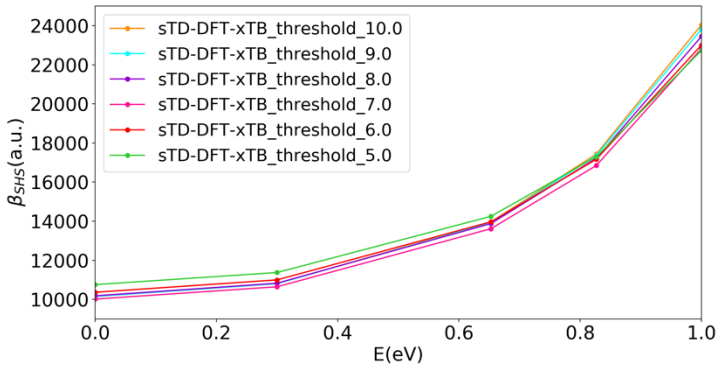

Figure S11: Tuning of the energy threshold E_{Th} for the supramolecular aggregate shown Figure S4b. In all sTD-DFT-xTB calculations, $y_J = 4.0$ and $y_K = 2.0$.

3. Optimization of the sTD-DFT-vTB parameters

We compare now the first hyperpolarizabilites calculated using the sTD-DFT-vTB method, restricted to valence-shell molecular orbitals, with those computed using the TD-DFT and sTD-DFT-xTB approaches. The y_J parameter is first tuned on the three test geometries of the isolated molecule, while y_K is kept fixed at 2.0. Figures S12, S13 and S14 show that reference TD-DFT β values are well reproduced when using $y_J = 0.4$, a much smaller value than that optimized in the case of sTD-DFT-xTB.

Then, the sTD-DFT-vTB method with $y_J = 0.4$ and $y_K = 2.0$ is tested using energy thresholds decreasing from 10 to 5 eV. As shown in Figures S15, S16 and S17, decreasing E_{th} slightly shifts upward the frequency dispersion curves, without any change in their shape. All E_{th} values provide frequency dispersion profiles of β in quite good agreement with TD-DFT, which allows us to consider the smallest E_{th} value for speeding up calculations. Again, the conclusion drawn for the isolated dyes can be extended to the case of larger aggregates, as shown in Figure S18. Therefore, one can conclude that a threshold of 5 eV can be used for sTD-DFT-vTB calculations on large aggregates.

Finally, the frequency dispersion curves of the first hyperpolarizability, calculated at the sTD-DFT-xTB ($y_J = 4.0$, $y_K = 2.0$ and $E_{th} = 6$ eV) and sTD-DFT-vTB ($y_J = 0.4$, $y_K = 2.0$ and $E_{th} = 5$ eV) levels for the three test geometries of the isolated molecule, are compared in Figure S19. Results obtained for the supramolecular aggregate are displayed in Figure S20. The curves show that restricting the MO space to the valence shell from sTD-DFT-xTB to sTD-DFT-vTB does not introduce significant loss in accuracy, while the execution times are reduced by a factor 2.

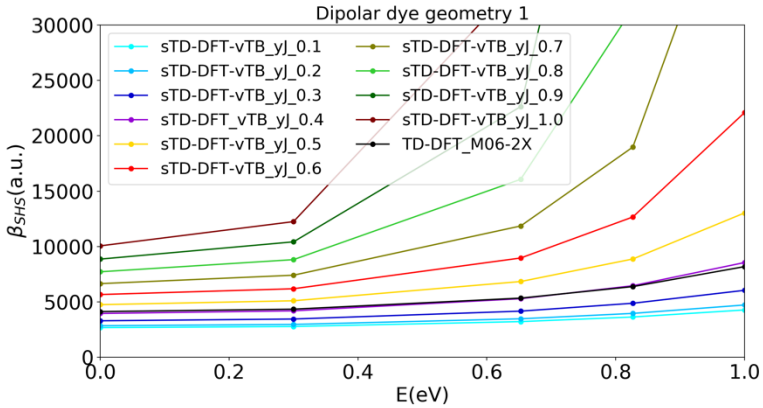

Figure S12: Tuning of the y_J parameter for the geometry 1 of the isolated molecule (Fig. S4a). In all sTD-DFT-vTB calculations, $y_K = 2.0$ and $E_{Th} = 10$ eV.

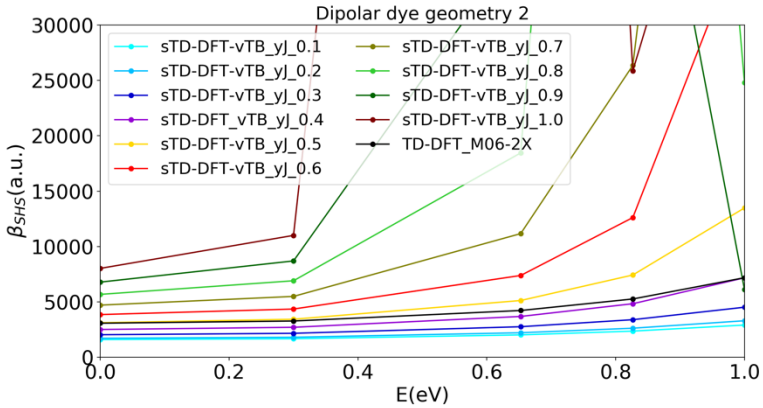

Figure S13: Tuning of the y_J parameter for the geometry 2 of the isolated molecule (Fig. S4a). In all sTD-DFT-vTB calculations, $y_K = 2.0$ and $E_{Th} = 10$ eV.

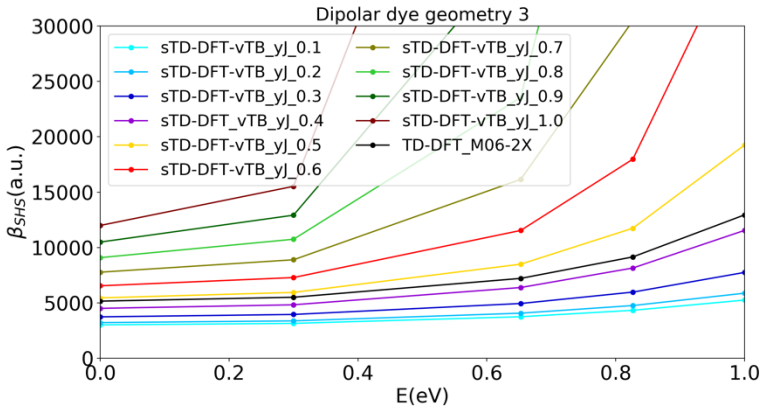

Figure S14: Tuning of the y_J parameter for the geometry 3 of the isolated molecule (Fig. S4a). In all sTD-DFT-vTB calculations, $y_K = 2.0$ and $E_{Th} = 10$ eV.

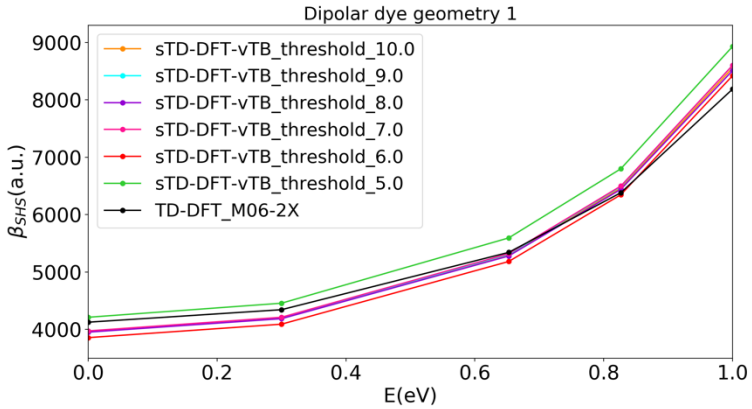

Figure S15: Tuning of the energy threshold E_{Th} for the geometry 1 of the isolated molecule (Fig. S4a). In all sTD-DFT-vTB calculations, $y_J = 0.4$ and $y_K = 2.0$.

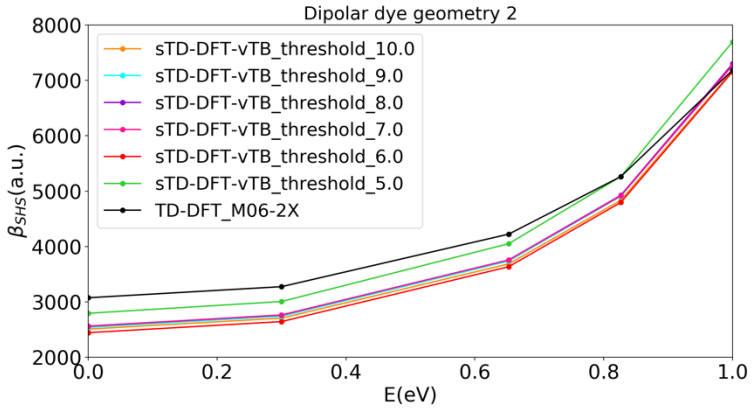

Figure S16: Tuning of the energy threshold E_{Th} for the geometry 2 of the isolated molecule (Fig. S4a). In all sTD-DFT-vTB calculations, $y_J = 0.4$ and $y_K = 2.0$.

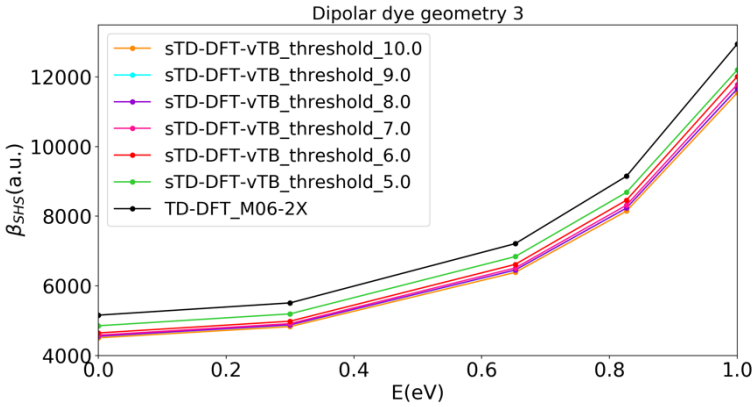

Figure S17: Tuning of the energy threshold E_{Th} for the geometry 3 of the isolated molecule (Fig. S4a). In all sTD-DFT-vTB calculations, $y_J = 0.4$ and $y_K = 2.0$.

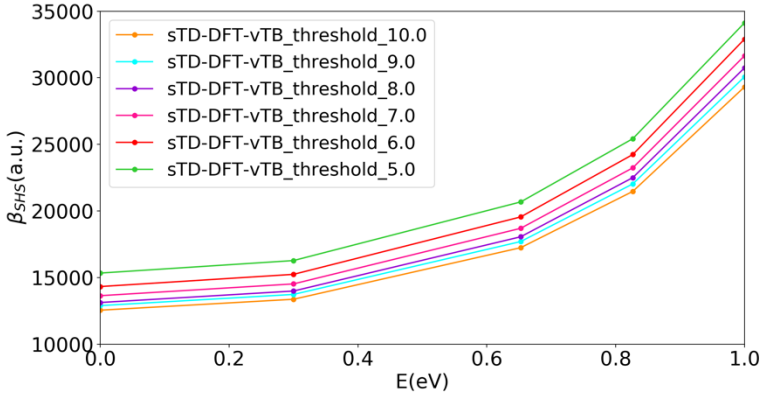

Figure S18: Tuning of the energy threshold E_{Th} for the supramolecular aggregate shown Figure S4b. In all sTD-DFT-vTB calculations, $y_J = 0.4$ and $y_K = 2.0$.

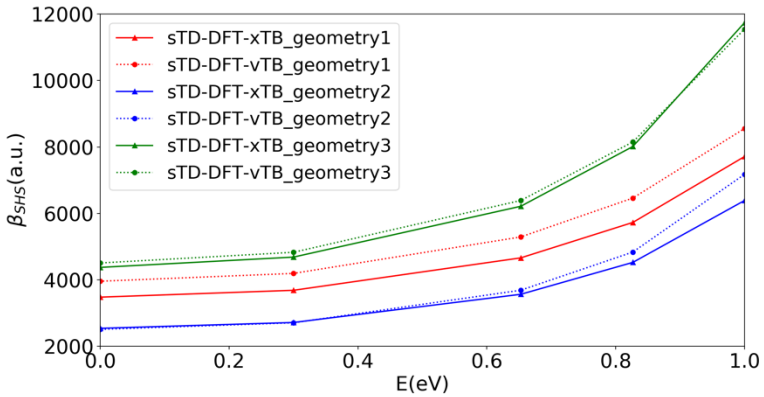

Figure S19: Frequency dispersion curves of the first hyperpolarizability for the three test geometries of the isolated molecule (Fig. S4a), as calculated at the sTD-DFT-xTB ($y_J = 4.0$, $y_K = 2.0$ and $E_{th} = 6$ eV) and sTD-DFT-vTB ($y_J = 0.4$, $y_K = 2.0$ and $E_{th} = 5$ eV) levels.

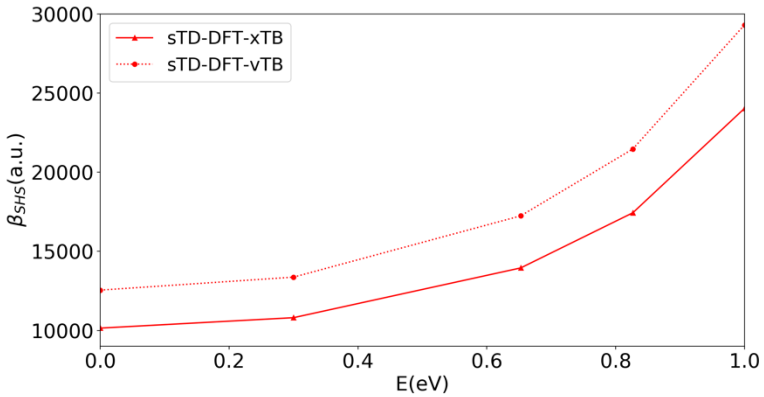

Figure S20: Frequency dispersion curves of the first hyperpolarizability for the supramolecular aggregate (Fig. S4b), as calculated at the sTD-DFT-xTB ($y_J = 4.0$, $y_K = 2.0$ and $E_{th} = 6$ eV) and sTD-DFT-vTB ($y_J = 0.4$, $y_K = 2.0$ and $E_{th} = 5$ eV) levels.

III. Free energy of pairs of chromophores in water

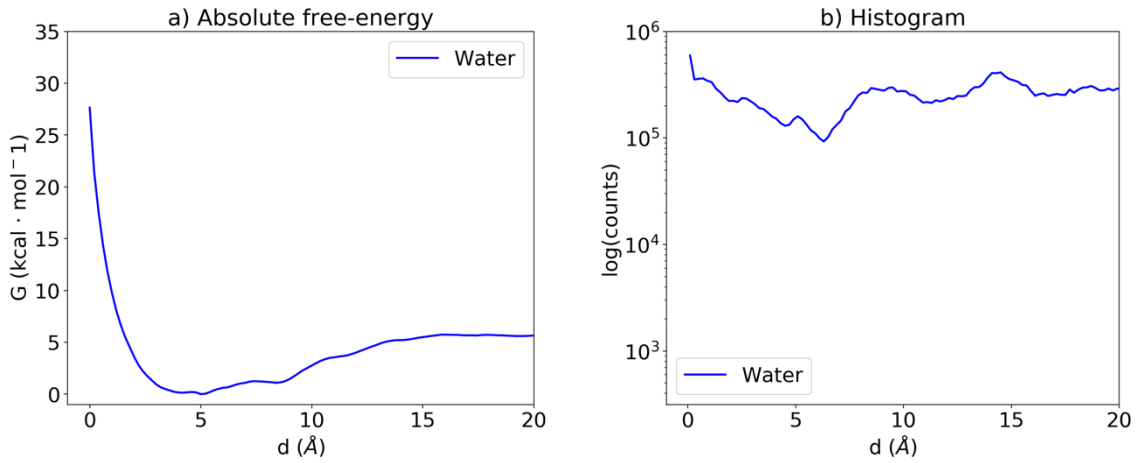

Figure S21: Free-energy as a function of the distance *d* between mass centers of the two dyes (a), as well as counts of distance values along the dynamics, showing that every distance *d* is statistically explored. Simulations at equilibrium were run for 20 ns on boxes containing two dipolar dyes in solvent, using the NpT ensemble at p = 1.01325 bar and T = 300 K, and the adaptive biasing force method for the calculation of free energy [S6].

IV. Morphology of the nanoparticles

1. Global shape of the nanoparticles

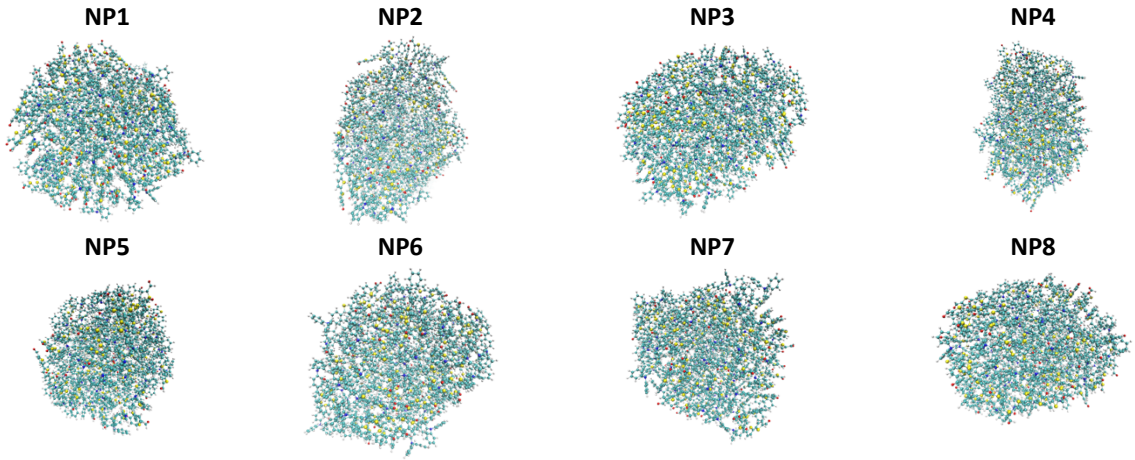

Figure S22: Shape of the nanoparticles issued from the 8 replicated MD trajectories.

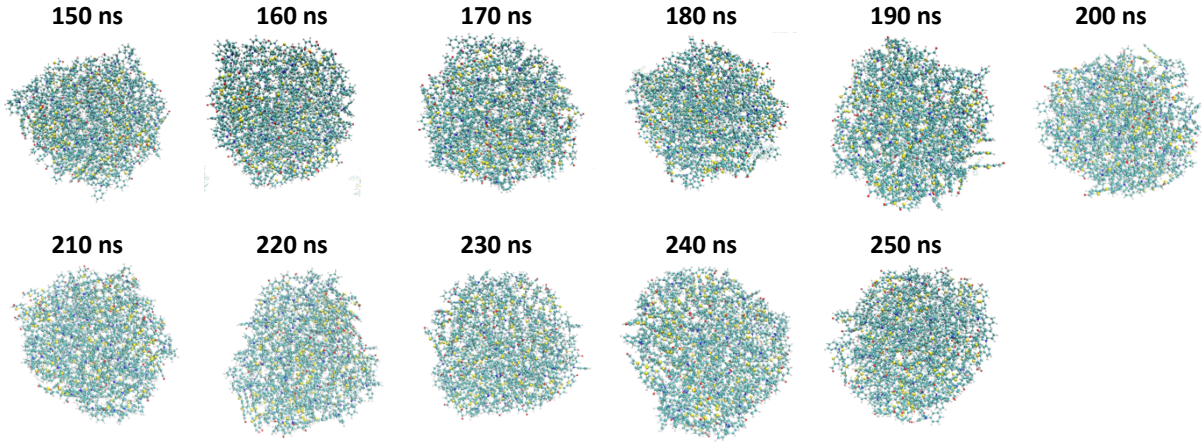

Figure S23: Time evolution of the shape of NP1 along the MD simulation.

2. Characterization of the shape of the nanoparticles

The moment of inertia tensor was calculated as a function of time for the largest nanoparticles for the 8 aggregation experiments and diagonalized, obtaining the eigenvalues $I_{zz} > I_{yy} > I_{xx}$, from which the corresponding component of the radius of gyration was obtained as $r_i = \sqrt{I_{ii}/M}$ where M is the NP mass (Figure S24). Following Varga and coworkers [S7], the shape of the particles was further characterized by calculating the two aspect ratios $\kappa_1 = r_z/r_x > \kappa_2 = r_z/r_y > 1$ and the biaxiality parameter $\theta = (\kappa_1 - 1)^{-1}(\kappa_1/\kappa_2 - \kappa_2)$, which takes the value of -1 for a perfectly uniaxial disc, $+1$ for a perfectly uniaxial rod, and 0 for a perfectly biaxial ellipsoid (Table S3). Most NPs assume nearly spherical shape (with aspect ratios close to 1) with a certain disc-like character $\theta < 0$), without any evident correlation between the orientation of the electric dipole moment and the ones the principal inertia axes, although a much larger number of simulations would be needed to confirm this result.

Table S3: Components of the radius of gyration (r_i, in Å), aspect ratios (κ_1, and κ_2) and biaxiality parameter θ, calculated over the last 50 ns of the trajectories for each NP, and (last line) averaged over the 8 NPs.

	r_x	r_y	r_z	κ_1	κ_2	θ
NP1	14.3 ± 0.1	14.5 ± 0.1	15.6 ± 0.3	1.10 ± 0.02	1.02 ± 0.01	0.6 ± 0.3
NP2	13.5 ± 0.2	15.5 ± 0.2	16.2 ± 0.2	1.20 ± 0.02	1.15 ± 0.02	-0.5 ± 0.1
NP3	12.8 ± 0.2	16.1 ± 0.3	16.8 ± 0.2	1.32 ± 0.03	1.25 ± 0.04	-0.6 ± 0.1
NP4	13.2 ± 0.1	15.8 ± 0.1	16.7 ± 0.2	1.26 ± 0.01	1.20 ± 0.02	-0.5 ± 0.1
NP5	13.7 ± 0.1	15.1 ± 0.1	15.7 ± 0.1	1.15 ± 0.02	1.10 ± 0.02	-0.4 ± 0.1
NP6	13.9 ± 0.2	15.1 ± 0.2	15.5 ± 0.1	1.12 ± 0.02	1.09 ± 0.02	-0.6 ± 0.2
NP7	13.5 ± 0.1	15.6 ± 0.1	15.9 ± 0.2	1.17 ± 0.02	1.15 ± 0.02	-0.7 ± 0.1
NP8	13.8 ± 0.1	14.9 ± 0.1	16.0 ± 0.1	1.16 ± 0.01	1.08 ± 0.01	0.0 ± 0.1
Av.	13.6 ± 0.4	15.3 ± 0.5	16.0 ± 0.5	1.18 ± 0.07	1.13 ± 0.07	-0.4 ± 0.4

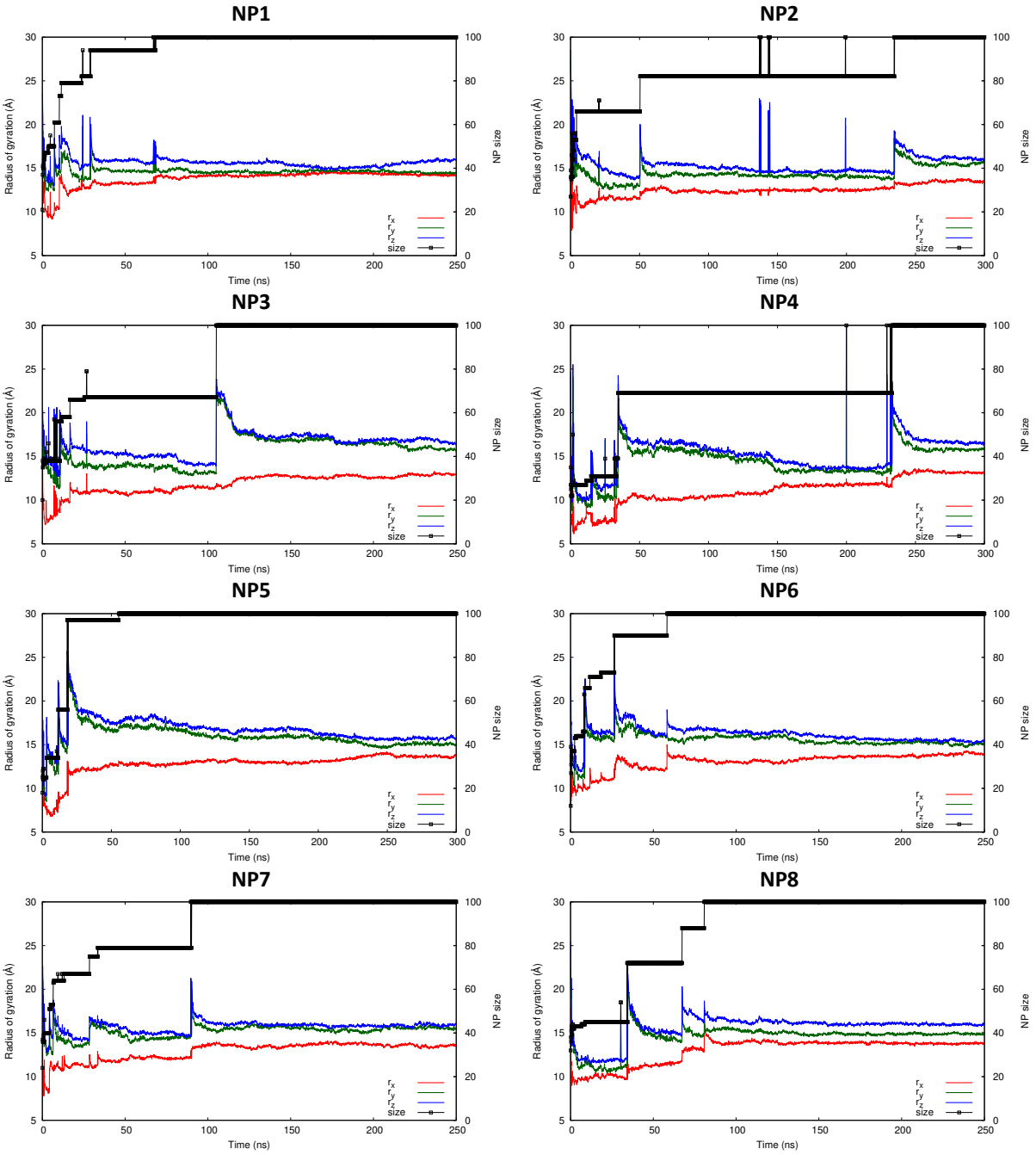

Figure S24: Time-evolution of the size and radius of gyration of the biggest nanoparticle with simulation time for the 8 replicated MD simulations.

3. Time-evolution and statistical distributions of structural and electronic properties

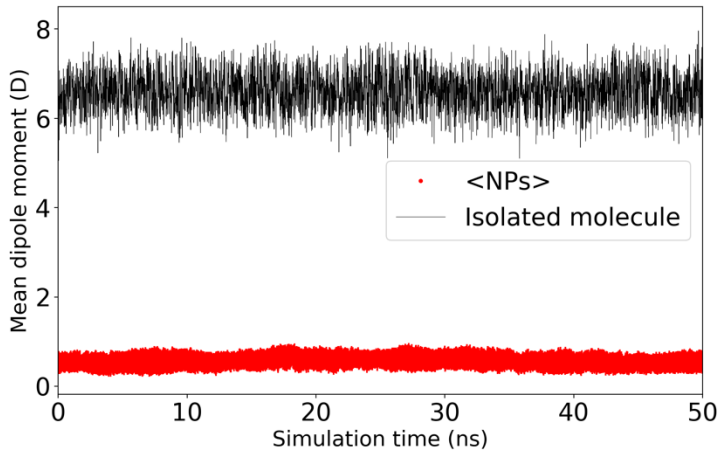

Figure S25: Evolution of the mean dipole moment with simulation time of an isolated dye and of the nanoparticles, divided by the number of their constitutive dyes.

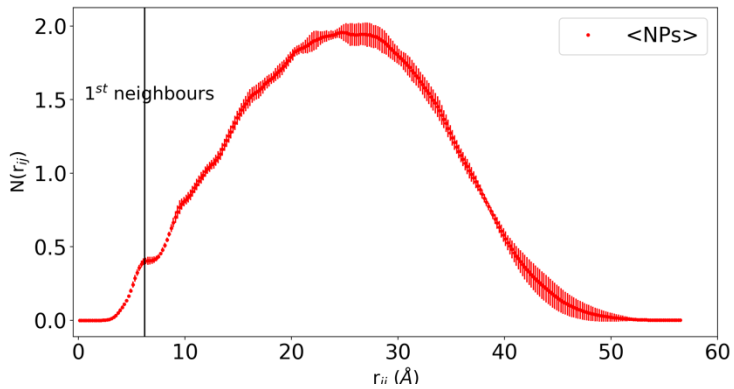

Figure S26: evolution of the mean density of neighbours as a function of the distance r_{ij} between the centers of mass of molecules.

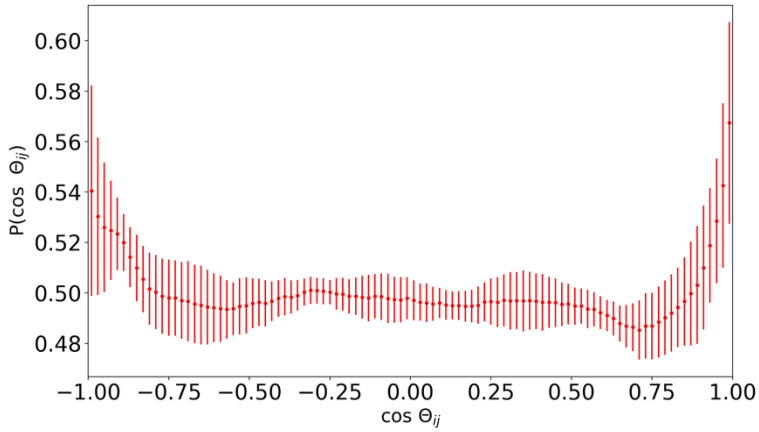

Figure S27: Distribution of $\cos\theta_{ij}$, where θ_{ij} is the angle between the dipole moment vectors of any pair of dyes at a distance lower than 7.5 Å.

4. π-aggregation of the molecular units

In this section, the π-stacking of the molecular units within the NP is investigated, using the following definitions:

Neighbour: a molecule with at least one non-H atom at a distance lower than 4 Å from the non-H atoms of the target molecule.

π-stacked neighbour: a molecule which is neighbour and has at least ten interatomic distances below 4 Å. Only distances between atoms 14, 15, 16, 17, 18, 19, 20, 35, 36, 37, 38, 41, 42, 43, 44, 45 of the two molecules are considered (see the scheme below for atom labels). Note that this is actually a loose definition, which includes also possible herringbone situations.

z-axis: unit vector parallel to the atom 14-atom 43 distance vector.
y-axis: unit vector perpendicular to z, obtained from the atom 35-atom 37 distance vector (removing its projection along z).

Relative orientation of π-stacked neighbours: defined by the scalar products between the unit vectors of the pair of interacting molecules:

$$\vec{z}_1 \cdot \vec{z}_2 = \cos(\vec{z}_1, \vec{z}_2)$$

$$|\vec{y}_1 \cdot \vec{y}_2| = |\cos(\vec{y}_1, \vec{y}_2)|$$

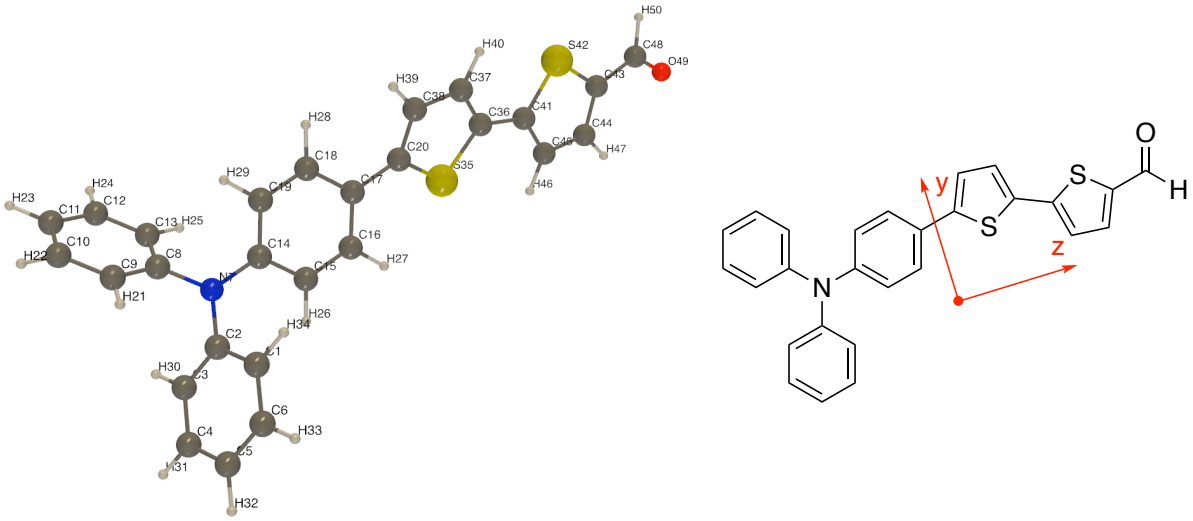

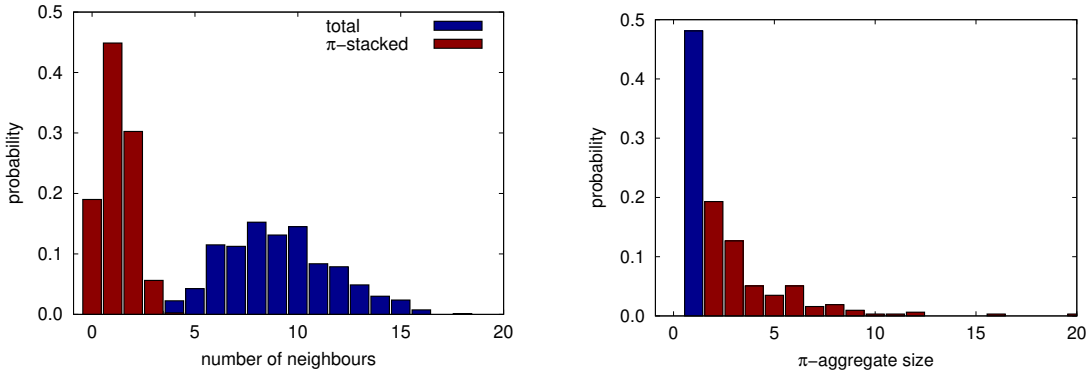

Figure S28: Left: Probability distribution of the number of neighbours (blue) and of the number of π-stacked neighbours (red), assuming the definitions given in the text. Values averaged over the 100 molecules of the 8 final nanoparticles (NP1-NP8). Right: Probability distribution of the number of molecules in the π-stacked aggregates. The blue box on the left panel corresponds to molecules that do not have π-stacked neighbours.

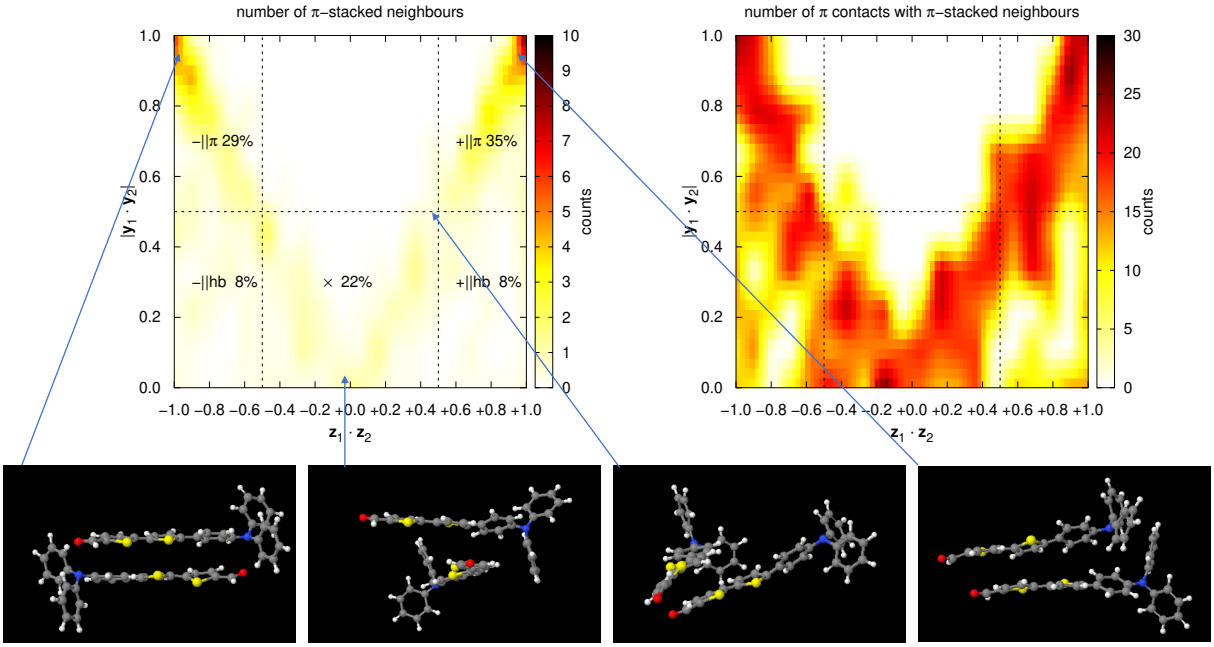

Figure S29: Number of π-stacked molecular pairs as a function of their relative orientation (see the definitions given in the text), as averaged over the 8 final nanoparticles (NP1-NP8). The labels on the left plot correspond to an arbitrary classification of the relative orientation of the long axes of the pair as parallel (+)/ antiparallel (-) or perpendicular (x), and of the short axes as π-stacked (π) or herringbone (hb).

V. Expression of the HRS invariants in terms of molecular β-tensor components

$$\begin{aligned}\left\langle \beta_{ZZZ}^2 \right\rangle = &\frac{1}{7}\sum_{\zeta}^{x,y,z}\beta_{\zeta\zeta\zeta}^2 + \frac{4}{35}\sum_{\zeta\neq\eta}^{x,y,z}\beta_{\zeta\zeta\eta}^2 + \frac{2}{35}\sum_{\zeta\neq\eta}^{x,y,z}\beta_{\zeta\zeta\zeta}\beta_{\zeta\eta\eta} + \frac{4}{35}\sum_{\zeta\neq\eta}^{x,y,z}\beta_{\eta\zeta\zeta}\beta_{\zeta\zeta\eta} \\ &+ \frac{4}{35}\sum_{\zeta\neq\eta}^{x,y,z}\beta_{\zeta\zeta\zeta}\beta_{\eta\eta\zeta} + \frac{1}{35}\sum_{\zeta\neq\eta}^{x,y,z}\beta_{\eta\zeta\zeta}^2 + \frac{4}{105}\sum_{\zeta\neq\eta\neq\xi}^{x,y,z}\beta_{\zeta\zeta\eta}\beta_{\eta\xi\xi} + \frac{1}{105}\sum_{\zeta\neq\eta\neq\xi}^{x,y,z}\beta_{\eta\zeta\zeta}\beta_{\eta\xi\xi} \\ &+ \frac{4}{105}\sum_{\zeta\neq\eta\neq\xi}^{x,y,z}\beta_{\zeta\zeta\eta}\beta_{\xi\xi\eta} + \frac{2}{105}\sum_{\zeta\neq\eta\neq\xi}^{x,y,z}\beta_{\zeta\eta\xi}^2 + \frac{4}{105}\sum_{\zeta\neq\eta\neq\xi}^{x,y,z}\beta_{\zeta\eta\xi}\beta_{\eta\zeta\xi}\end{aligned} \tag{S1}$$

$$\begin{aligned}\left\langle \beta_{ZXX}^2 \right\rangle = &\frac{1}{35}\sum_{\zeta}^{x,y,z}\beta_{\zeta\zeta\zeta}^2 + \frac{4}{105}\sum_{\zeta\neq\eta}^{x,y,z}\beta_{\zeta\zeta\zeta}\beta_{\zeta\eta\eta} - \frac{2}{35}\sum_{\zeta\neq\eta}^{x,y,z}\beta_{\zeta\zeta\zeta}\beta_{\eta\eta\zeta} + \frac{8}{105}\sum_{\zeta\neq\eta}^{x,y,z}\beta_{\zeta\zeta\eta}^2 \\ &+ \frac{3}{35}\sum_{\zeta\neq\eta}^{x,y,z}\beta_{\zeta\eta\eta}^2 - \frac{2}{35}\sum_{\zeta\neq\eta}^{x,y,z}\beta_{\zeta\zeta\eta}\beta_{\eta\zeta\zeta} + \frac{1}{35}\sum_{\zeta\neq\eta\neq\xi}^{x,y,z}\beta_{\zeta\eta\eta}\beta_{\zeta\xi\xi} - \frac{2}{105}\sum_{\zeta\neq\eta\neq\xi}^{x,y,z}\beta_{\zeta\zeta\xi}\beta_{\eta\eta\xi} \\ &- \frac{2}{105}\sum_{\zeta\neq\eta\neq\xi}^{x,y,z}\beta_{\zeta\zeta\eta}\beta_{\eta\xi\xi} + \frac{2}{35}\sum_{\zeta\neq\eta\neq\xi}^{x,y,z}\beta_{\zeta\eta\xi}^2 - \frac{2}{105}\sum_{\zeta\neq\eta\neq\xi}^{x,y,z}\beta_{\zeta\eta\xi}\beta_{\eta\zeta\xi}\end{aligned} \tag{S2}$$

$$\begin{aligned}\left\langle \left(\beta_{ZXZ}+\beta_{ZZX}\right)^2 - 2\beta_{ZZZ}\beta_{ZXX} \right\rangle = &\frac{3}{35}\sum_{\zeta}^{x,y,z}\beta_{\zeta\zeta\zeta}^2 - \frac{1}{105}\sum_{\zeta\neq\eta}^{x,y,z}\beta_{\zeta\zeta\zeta}\beta_{\zeta\eta\eta} + \frac{2}{70}\sum_{\zeta\neq\eta}^{x,y,z}\beta_{\zeta\zeta\zeta}\beta_{\eta\eta\zeta} + \frac{38}{105}\sum_{\zeta\neq\eta}^{x,y,z}\beta_{\zeta\zeta\eta}^2 \\ &+ \frac{2}{35}\sum_{\zeta\neq\eta}^{x,y,z}\beta_{\zeta\eta\eta}^2 + \frac{2}{70}\sum_{\zeta\neq\eta}^{x,y,z}\beta_{\zeta\zeta\eta}\beta_{\eta\zeta\zeta} - \frac{1}{21}\sum_{\zeta\neq\eta\neq\xi}^{x,y,z}\beta_{\zeta\eta\eta}\beta_{\zeta\xi\xi} + \frac{8}{105}\sum_{\zeta\neq\eta\neq\xi}^{x,y,z}\beta_{\zeta\zeta\xi}\beta_{\eta\eta\xi} \\ &- \frac{13}{105}\sum_{\zeta\neq\eta\neq\xi}^{x,y,z}\beta_{\zeta\zeta\eta}\beta_{\eta\xi\xi} + \frac{11}{105}\sum_{\zeta\neq\eta\neq\xi}^{x,y,z}\beta_{\zeta\eta\xi}^2 + \frac{8}{105}\sum_{\zeta\neq\eta\neq\xi}^{x,y,z}\beta_{\zeta\eta\xi}\beta_{\eta\zeta\xi}\end{aligned} \tag{S3}$$

$$\left|\beta_{J=1}\right|^2 = 6\left\langle \beta_{ZZZ}^2 \right\rangle - 9\left\langle \beta_{ZXX}^2 \right\rangle \tag{S4}$$

$$\left|\beta_{J=3}\right|^2 = -\frac{7}{2}\left\langle \beta_{ZZZ}^2 \right\rangle + \frac{9}{5}\left\langle \beta_{ZXX}^2 \right\rangle \tag{S5}$$

VI. NLO properties of the nanoparticles

5. NLO properties of the final nanoparticles of each MD run

Table S4: Static first hyperpolarizabilities (β_{HRS}, in 10^3 a.u.) and depolarization ratios (DR) of the final nanoparticles issued from the 8 replicated MD trajectories (Figure S21), evaluated using the tensor sum approximation at the TD-DFT and sTD-DFT-vTB levels, as well as from sTD-DFT-vTB calculations performed on the full nanoparticles.

	TD-DFT[a] (tensor sum)		sTD-DFT-vTB[b] (tensor sum)		sTD-DFT-vTB[b] (full calculation)			
	β_{HRS}	DR	β_{HRS}	DR	β_{HRS}	DR	R_1[c]	R_2[d]
NP1	58.3	5.5	55.2	4.9	45.9	4.8	0.9	0.83
NP2	23.4	2.9	22.1	3.4	22.4	4.3	0.9	1.01
NP3	31.4	4.1	31.1	4.3	19.6	2.7	1.0	0.63
NP4	39.0	5.1	31.5	4.3	25.2	5.1	0.8	0.80
NP5	56.1	5.6	63.7	6.3	55.5	6.2	1.1	0.87
NP6	47.9	3.7	51.5	4.4	40.4	4.4	1.1	0.78
NP7	46.8[e]	3.6[e]	44.9	4.2	34.3	4.7	1.0	0.76
NP8	47.8	5.6	43.0	5.0	33.5	5.1	0.9	0.78
av. ± std. dev.	43.8 ± 11.9	4.5 ± 1.1	42.9 ± 14.0	4.6 ± 0.8	34.6 ± 12.3	4.7 ± 1.0	1.0 ± 0.10	0.8 ± 0.11

[a] M06-2X/6-311+G(d) in gas phase

[b] using $y_J = 0.4$, $y_K = 2.0$ and $E_{th} = 5.0$ eV

[c] $R_1 = \beta_{HRS}^{\mathrm{sTD-DFT-vTB}}(tensor\ sum)/\beta_{HRS}^{\mathrm{TD-DFT}}(tensor\ sum)$

[d] $R_2 = \beta_{HRS}^{\mathrm{sTD-DFT-vTB}}(full\ calc.)/\beta_{HRS}^{\mathrm{sTD-DFT-vTB}}(tensor\ sum)$

[e] one molecule was removed from the calculations due to numerical instability

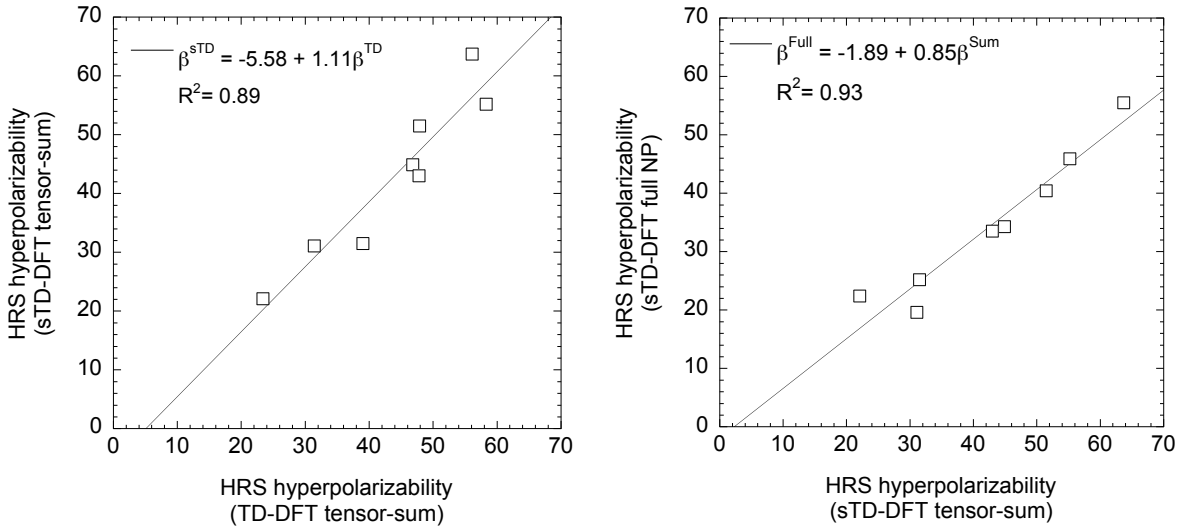

Figure S30: Linear correlations between (a) static first hyperpolarizabilities (in 10^3 a.u.) evaluated using the tensor sum approximation at the TD-DFT and sTD-DFT-vTB levels, and between (b) sTD-DFT-vTB static first hyperpolarizabilities calculated using the tensor sum approximation and calculations performed on the full nanoparticles.

Table S5: Dynamic (λ = 1064 nm) first hyperpolarizabilities (β_{HRS}, in 10^3 a.u.) and depolarization ratios (DR) of the final nanoparticles issued from the 8 replicated MD trajectories (Figure S21), evaluated using the tensor sum approximation at the TD-DFT and sTD-DFT-vTB levels, as well as from sTD-DFT-vTB calculations performed on the full nanoparticles.

	TD-DFT[a] (tensor sum)		sTD-DFT-vTB[b] (tensor sum)		sTD-DFT-vTB[b] (full calculation)			
	β_{HRS}	DR	β_{HRS}	DR	β_{HRS}	DR	R_1[c]	R_2[d]
NP1	317.0	6.3	325.8	5.8	3194.5	4.8	1.0	9.81
NP2	112.0	3.7	248.2	3.4	106.4	3.0	2.2	0.43
NP3	110.7	3.0	161.2	3.8	616.9	3.6	1.5	3.83
NP4	160.1	5.1	238.9	5.2	2259.4	5.1	1.5	9.46
NP5	237.6	5.9	343.1	7.2	369.9	4.7	1.4	1.08
NP6	185.0	3.6	238.7	4.5	212.7	4.9	1.3	0.89
NP7	234.0	3.4	827.6	5.0	156.6	2.1	3.5	0.19
NP8	156.4	5.5	167.9	5.3	634.3	5.0	1.1	3.78
av. ± std. dev.	189.1 ± 70.5	4.6 ± 1.3	318.9 ± 215.4	5.0 ± 1.2	943.8 ± 1145.4	4.2 ± 1.1	/	/

[a] M06-2X/6-311+G(d) in gas phase

[b] using γ_J = 0.4, γ_K = 2.0 and E_{th} = 5.0 eV

[c] $R_1 = \beta_{HRS}^{\mathrm{sTD-DFT-vTB}}(tensor\ sum)/\beta_{HRS}^{\mathrm{TD-DFT}}(tensor\ sum)$

[d] $R_2 = \beta_{HRS}^{\mathrm{sTD-DFT-vTB}}(full\ calc.)/\beta_{HRS}^{\mathrm{sTD-DFT-vTB}}(tensor\ sum)$

6. Evolution in time of the NLO properties

Table S6: Evolution in time of the dynamic (λ = 1064 nm) first hyperpolarizabilities (β_{HRS}, in 10^3 a.u.) and depolarization ratios (DR) of the nanoparticles along the 8 replicated MD trajectories, evaluated using the tensor sum approximation at the TD-DFT/M06-2X/6-311+G(d) level in gas phase. The starting time is taken when the 100 molecules collapse into a single structure.

NP1

Simulation time (ns)	β_{HRS}	DR
100	104.2	2.0
110	111.5	3.5
120	95.0	5.1
130	172.9	5.8
140	77.9	3.7
150	119.3	3.4
160	102.3	3.5
170	118.6	2.5
180	89.6	3.6
190	102.3	3.9
200	196.1	5.8
210	223.9	4.9
220	260.6	6.4
230	115.5	4.7
240	193.8	6.5
250	317.0	6.3
av. ± std. dev.	156.1 ± 72.9	4.48 ± 1.42

NP2

Simulation time (ns)	β_{HRS}	DR
250	178.8	4.9
260	172.3	8.7
270	234.4	5.6
280	142.7	2.5
290	116.1	2.9
300	112.0	3.7
av. ± std. dev.	172.7 ± 70.1	4.72 ± 2.28

NP3

Simulation time (ns)	β_{HRS}	DR
190	126.8	2.3
200	126.3	2.7
210	155.2	1.9
220	142.3	5.0
230	165.3	5.5
240	162.6	4.8
250	110.7	3.0
av. ± std. dev.	132.7 ± 30.5	3.6 ± 1.5

NP4

Simulation time (ns)	β_{HRS}	DR
250	140.9	2.1
260	156.8	2.8
270	105.8	3.0
280	205.0	3.0
290	111.4	2.0
300	160.1	5.1
av. ± std. dev.	135.3 ± 43.4	3.0 ± 1.1

NP5

Simulation time (ns)	β_{HRS}	DR
140	186.4	4.3
150	197.4	3.3
160	171.4	3.1
170	166.5	4.2
180	184.8	3.3
190	190.3	3.6
200	215.5	4.1
210	285.4	6.8
220	230.3	3.5
230	243.6	5.4
240	198.9	5.4
250	204.6	5.1
260	155.5	3.2
270	171.9	3.7
280	232.5	4.0
290	144.1	3.6
300	237.6	5.9
av. ± std. dev.	204.4 ± 39.1	4.3 ± 1.1

NP6

Simulation time (ns)	β_{HRS}	DR
140	251.0	7.0
150	116.4	5.8
160	137.4	3.8
170	167.2	4.3
180	175.0	6.1
190	211.6	5.3
200	115.5	1.7
210	179.7	3.0
220	179.8	2.2
230	208.6	3.4
240	170.9	4.6
250	185.0	3.6
av. ± std. dev.	174.8 ± 39.1	4.2 ± 1.6

NP7

Simulation time (ns)	β_{HRS}	DR
130	267.7	5.7
140	188.4	4.1
150	277.8	7.0
160	166.4	3.4
170	207.2	4.6
180	178.7	3.6
190	206.6	3.4
200	203.9	5.1
210	318.6	8.1
220	242.0	7.3
230	356.7	6.4
240	180.8	4.4
250	234.0	3.4
av. ± std. dev.	233.0 ± 57.9	5.1 ± 1.6

NP8

Simulation time (ns)	β_{HRS}	DR
120	134.8	3.5
130	102.2	1.8
140	157.7	2.5
150	161.9	4.8
160	171.2	4.9
170	156.8	6.7
180	178.2	6.6
190	116.2	2.9
200	215.4	7.7
210	179.9	6.6
220	143.4	4.2
230	238.7	7.1
240	193.3	4.2
250	156.4	5.5
av. ± std. dev.	164.7 ± 36.3	4.9 ± 1.8

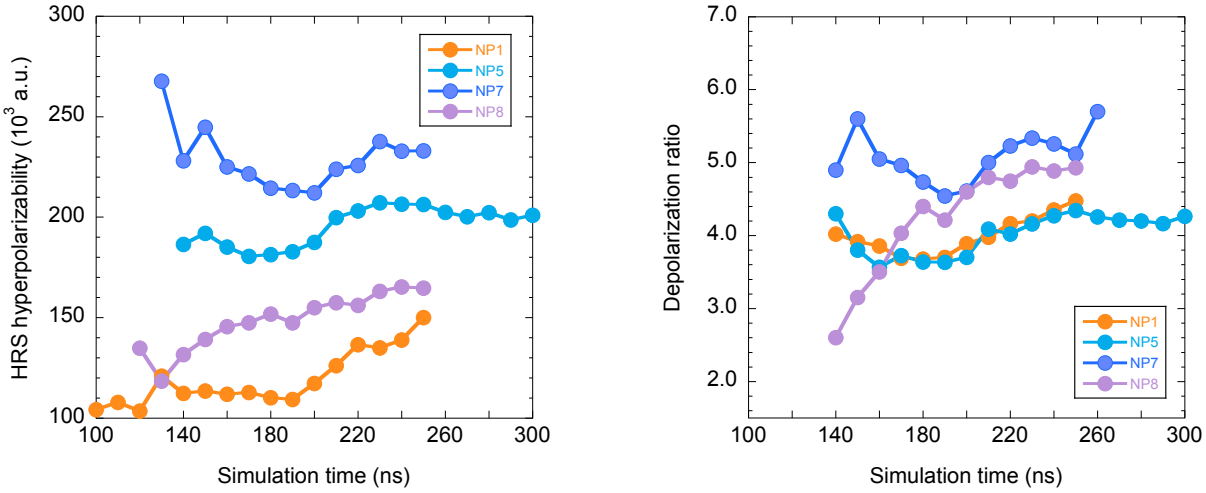

Figure S31: Time evolution of the cumulative averages of β_{HRS} (left) and DR (right) values for NP1, 5 7 and 8, as calculated using the tensor-sum approximation at the TD-DFT:M06-2X/6-311+G(d) level.

VII. Absorption properties of π-stacked dimers

1. Comparison between TD-DFT and sTD-DFT-vTB calculations

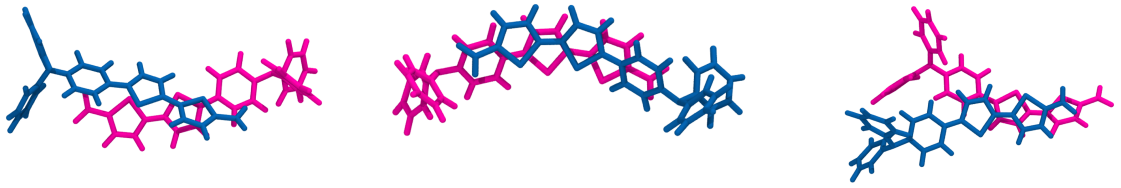

D1 **D2** **D3**

Figure S32: Representative π-stacked dimer structures extracted from the NPs.

Table S7: Excitation energies (ΔE, eV) and oscillator strengths (f) associated to the main low-lying $S_0 \rightarrow S_i$ electronic transitions ($\Delta E \leq 4$ eV, $f \geq 0.1$) calculated for the isolated dye and of the π-stacked dimers.

	TD-DFT [a]			sTD-DFT-vTB [b]		
	S_i	ΔE	f	S_i	ΔE	f
Monomer [c]	S_1	3.15	1.28	S_1	3.17	1.16
D1	S_1	2.74	0.10	S_3	3.07	0.24
	S_2	3.05	1.81	S_3	3.34	2.59
	S_3	3.23	0.23	S_3	3.73	0.17
D2	S_2	2.85	1.30	S_3	2.86	0.21
	S_3	3.14	0.58	S_4	3.24	1.20
	S_4	3.30	0.09	S_5	3.40	1.22
				S_6	3.80	0.13
D3	S_1	2.49	0.82	S_1	2.58	1.14
	S_3	3.10	1.25	S_4	3.32	1.54
				S_5	3.54	0.10

[a] M06-2X/6-311+G(d) calculations in B3LYP/cc-pVTZ geometry. [b] Using $y_J = 4.0$, $y_K = 2.0$ and $E_{th} = 5.0$ eV. [c] In the trans form.

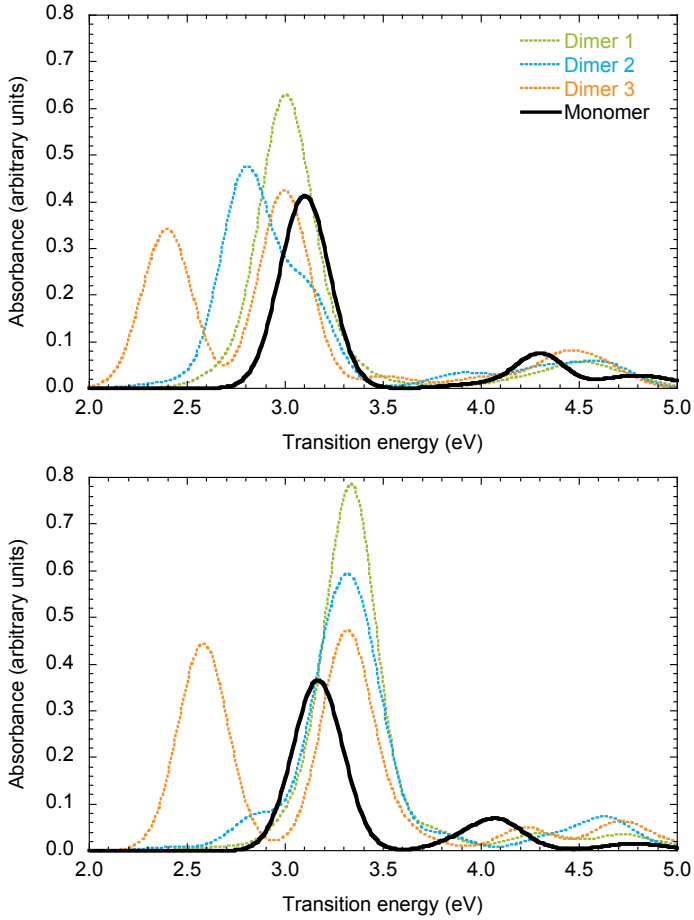

Figure S33: Absorption spectra of π-stacked dimer structures represented in Figure S32, calculated at the TD-DFT (top) and sTD-DFT-vTB (bottom) levels.

2. Diabatization of low-lying excited states

Diabatization of the electronic transitions was performed for singlet excited states of three representative π-stacked dimers extracted from the NPs (Figure 10, main text), by means of the Boys localization scheme [S8] implemented in the Q-Chem program. [S9] Computation of the diabatic states ({Zi}) was performed on the basis of adiabatic states calculated in vacuum at the M06-2X/6-311+G(d) level using the Tamm–Dancoff approximation (TDA) [S10], since the localization scheme is not implemented for TD-DFT states. The number of adiabatic states considered corresponds to the number of intramolecular and intermolecular charge-transfer contributions. In practice, only the lowest 4 excited singlets (S1-S4) involving transitions from the HOMO-1 and HOMO to the LUMO and LUMO+1 were considered for dimers D1 and D2. For D3, S5 has been considered instead of S4.

Dimer D1

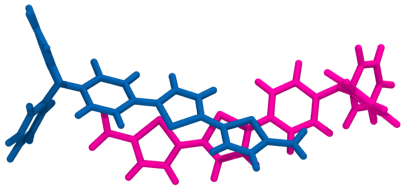

Table S8a: Energies of adiabatic (Si) states (in eV), oscillator strengths, and contributions of electronic excitations (in %) in dimer **D1**, as calculated using TD-DFT and TDA. H = HOMO; L = LUMO.

	TD-DFT		TDA		
	ΔE	*f*	ΔE	*f*	contributions
S_1	2.742	0.098	2.849	0.096	81% H → L
S_2	3.053	1.810	3.191	1.242	82% H → L+1 08% H → L
S_3	3.237	0.238	3.298	1.414	81% H-1 → L
S_4	3.442	0.076	3.466	0.213	81% H-1 → L+1 06% H-1 → L

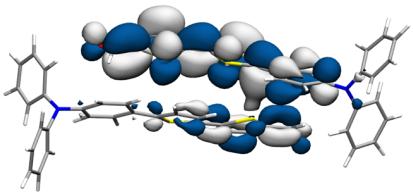

LUMO

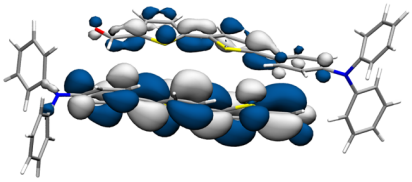

LUMO+1

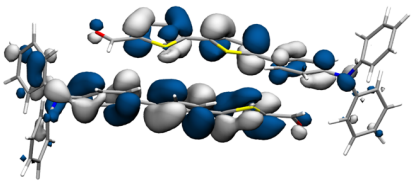

HOMO

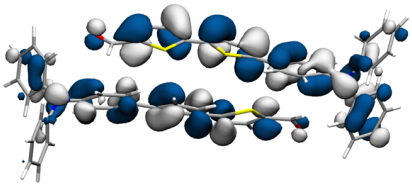

HOMO-1

Figure S34: Sketch of the frontier orbitals of dimer **D1**.

Table S8b: Energies of the TDA adiabatic (Si) states (in eV, oscillator strength in parenthesis) of dimer **D1**, and their diabatic composition in terms of intra (in blue) and intermolecular (in orange) contributions and Z_i states: $Z_{intra} = Z_1 + Z_2$ and $Z_{inter} = Z_3 + Z_4$.

i	S_i	Z_{intra}	Z_{inter}	Z_1	Z_2	Z_3	Z_4
1	2.85 (0.10)	**73**	27	47	26	21	6
2	3.19 (1.24)	52	48	6	47	34	13
3	3.30 (1.41)	57	43	47	10	43	0
4	3.47 (0.21)	18	**82**	1	17	1	81

Table S8c: Excitation energy (in eV) and relative Mulliken fragment charges of diabatic states of dimer **D1** with respect to the ground state charge distribution.

			molecule 1		molecule 2	
i	Z_i	nature	e-	h+	e-	h+
1	3.08	intra	-0.0251	0.0233	**-0.9748**	**0.9767**
2	3.16	intra	**-0.9758**	**0.9754**	-0.0239	0.0247
3	3.17	inter	-0.0387	**0.9652**	**-0.9615**	0.0344
4	3.39	inter	**-0.9766**	0.0409	-0.0231	**0.9589**

Dimer D2

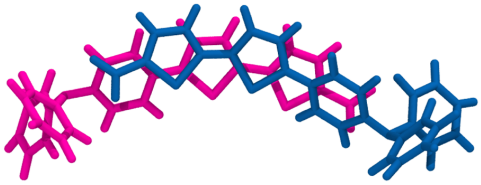

Table S9a: Energies of adiabatic (Si) states (in eV), oscillator strengths, and contributions of electronic excitations (in %) in dimer **D2**, as calculated using TD-DFT and TDA. H = HOMO; L = LUMO.

	TD-DFT		TDA		
	ΔE	*f*	ΔE	*f*	contributions
S_1	2.501	0.027	2.614	0.022	90% H → L
S_2	2.859	1.290	2.980	0.871	89% H → L+1
S_3	3.139	0.594	3.226	1.606	80% H-1 → L 05% H-1 → L+1
S_4	3.294	0.089	3.325	0.232	82% H-1 → L+1 06% H-1 → L 05% H-3 → L+1

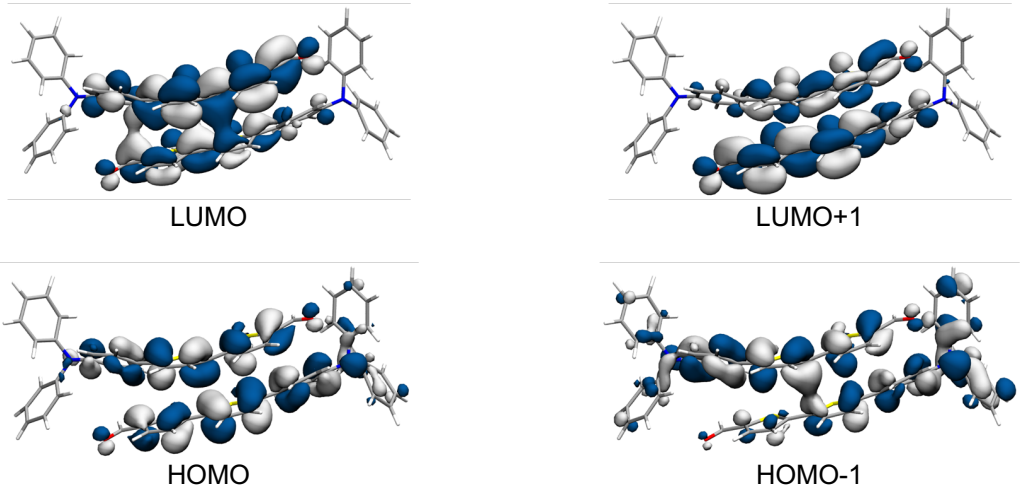

Figure S35: Sketch of the frontier orbitals of dimer **D2**.

Table S9b: Energies of TDA adiabatic (Si) states (in eV, oscillator strength in parenthesis) of dimer **D2**, and their diabatic composition in terms of intra (in blue) and intermolecular (in orange) contributions and Z_i states: $Z_{intra} = Z_1 + Z_3$ and $Z_{inter} = Z_2 + Z_4$.

i	S_i	Z_{intra}	Z_{inter}	Z_1	Z_2	Z_3	Z_4
1	2.61 (0.02)	**67**	33	41	20	26	13
2	2.98 (0.87)	36	**64**	9	37	28	27
3	3.23 (1.61)	**62**	38	47	37	15	1
4	3.33 (0.23)	34	**66**	3	7	31	59

Table S9c: Excitation energy (in eV) and relative Mulliken fragment charges of diabatic states of dimer **D2** with respect to the ground state charge distribution.

			molecule 1		molecule 2	
i	Z_i	nature	e-	h+	e-	h+
1	2.95	intra	**-0.9875**	**0.9706**	-0.0124	0.0293
2	3.02	inter	**-0.9935**	-0.0038	-0.0064	**1.0038**
3	3.03	intra	-0.0135	0.0055	**-0.9865**	**0.9945**
4	3.14	inter	-0.0151	**0.9779**	**-0.9853**	0.0218

Dimer D3

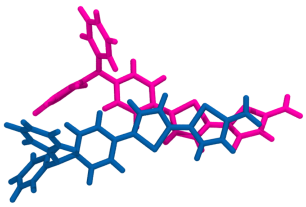

Table S10a: Energies of adiabatic (Si) states (in eV), oscillator strengths, and contributions of electronic excitations (in %) in dimer **D3**, as calculated using TD-DFT and TDA. H = HOMO; L = LUMO.

	TD-DFT		TDA		
	ΔE	*f*	ΔE	*f*	contributions
S_1	2.490	0.827	2.675	1.014	89% H → L
S_2	2.920	0.026	2.931	0.094	91% H-1 → L
S_3	3.106	1.262	3.239	1.712	47% H → L+1 38% H-1 → L+1
S_4	3.295	0.001	3.365	0.001	50% H-17 → L 29% H-17 → L+2
S_5	3.552	0.063	3.566	0.109	41% H-1 → L+1 39% H → L+1 05% H-18 → L+1

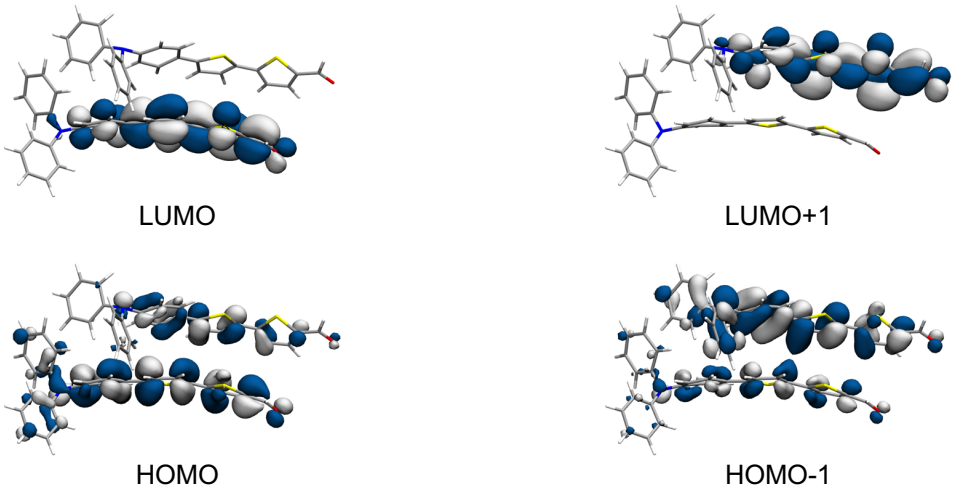

Figure S36: Sketch of the frontier orbitals of dimer **D3**.

Table S10b: Energies of TDA adiabatic (Si) states (in eV, oscillator strength in parenthesis) of dimer **D3**, and their diabatic composition in terms of intra (in blue) and intermolecular (in orange) contributions and Z_i states: $Z_{intra} = Z_1 + Z_3 + Z_4$ and $Z_{inter} = Z_2$.

i	S_i	Z_{intra}	Z_{inter}	Z_1	Z_2	Z_3	Z_4
1	2.67 (1.01)	**89**	11	83	11	5	0
2	2.93 (0.09)	11	**89**	11	89	0	0
3	3.24 (1.71)	**100**	0	4	0	87	9
5	3.57 (0.11)	**100**	0	1	0	7	91

Table S10c: Excitation energy (in eV) and relative Mulliken fragment charges of diabatic states of dimer **D3** with respect to the ground state charge distribution.

			molecule 1		molecule 2	
i	Z_i	nature	e-	h+	e-	h+
1	2.74	intra	**-0.8357**	**0.8358**	-0.1642	0.1639
2	2.90	inter	**-0.9929**	0.0023	-0.0078	**0.9981**
3	3.24	intra	-0.1860	0.1812	**-0.8140**	**0.8189**
5	3.54	intra	**-0.9995**	**0.9995**	-0.0003	0.0004

VIII. Assessment of M06-2X with respect to MP2

Table S11: Static β_{HRS} (a.u.) and DR values computed at the M06-2X/6-311G(d) and MP2/6-311G(d) levels, for the molecule in gas phase in the three geometries illustrated in Figure S4a.

	Geometry 1		Geometry 2		Geometry 3	
	β_{HRS}	DR	β_{HRS}	DR	β_{HRS}	DR
TD-DFT; M06-2X/6-311G(d); gas phase	4126	4.7	3075	4.4	5159	4.7
FF-MP2/6-311G(d); gas phase	4373	4.9	2651	4.5	4902	4.9

IX. References

[S1] Y. Wu, H. L. Tepper, and G. A. Voth. Flexible simple point-charge water model with improved liquid-state properties. The Journal of Chemical Physics, 124(2):024503, 2006.

[S2] AA. K. Soper, "The Radial Distribution Functions of Water as Derived from Radiation Total Scattering Experiments: Is There Anything We Can Say for Sure?", International Scholarly Research Notices, vol. 2013, Article ID 279463, 67 pages, 2013.

[S3] F. Fallahi and H. Mohammadi-Manesh. Molecular dynamics simulations of carbon monoxide self-diffusion in the nanoporous of the Cu-BTC. Procedia Materials Science, 11:449 – 453, 2015.

[S4] D. H. S. Ramkumar and A. P. Kudchadker. Mixture properties of the water + γ-butyrolactone + tetrahydrofuran system. Journal of Chemical & Engineering Data, 34(4):459–463, 1989.

[S5] S. H. Donaldson, J. P. Jahnke, R. J. Messinger, Å. Östlund, D. Uhrig, J. N. Israelachvili, and B. F. Chmelka. Correlated diffusivities, solubilities, and hydrophobic interactions in ternary polydimethylsiloxane–water–tetrahydrofuran mixtures. Macromolecules, 49(18):6910–6917, 2016.

[S6] J. Comer, J. C. Gumbart, J. Hénin, T. Lelièvre, A. Pohorille, C. Chipot. The adaptive biasing force method: Everything you always wanted to know but were afraid to ask. Journal of Physical Chemistry B, 119(3):1129–1151, 2015.

[S7] M. González-Pinto, Y. Martínez-Ratón, E. Velascoc, S. Vargad Phys. Chem. Chem. Phys., 2015,17, 6389-6400.

[S8] J. E. Subotnik, S. Yeganeh, R. J. Cave and M. A. Ratner, Constructing diabatic states from adiabatic states: Extending generalized Mulliken–Hush to multiple charge centers with Boys localization, J. Chem. Phys., 2008, 129, 244101.

[S9] Y. Shao, et al., Advances in molecular quantum chemistry contained in the Q-Chem 4 program package, Mol. Phys., 2015, 113, 184–215.

[S10] S. Hirata and M. Head-Gordon, Time-dependent density functional theory within the Tamm-Dancoff approximation, Chem. Phys. Lett., 1999, 314, 291–299.